Lawrence Berkeley National Laboratory

Title

Reviving the rock-salt phases in Ni-rich layered cathodes by mechano-electrochemistry in all-solid-state batteries

Permalink

https://escholarship.org/uc/item/6xw7s4mk

Authors

Wang, Zaifa

Wang, Zhenyu

Xue, Dingchuan

et al.

Publication Date

2023

DOI

10.1016/j.nanoen.2022.108016

Copyright Information

Peer reviewed

Reviving the rock-salt phases in Ni-rich layered cathodes by mechano-electrochemistry in all-solid-state batteries

Zaifa Wang[1,†], Zhenyu Wang[2,†], Dingchuan Xue[3], Jun Zhao[1], Xuedong Zhang[4], Lin Geng[1], Yanshuai Li[1], Congcong Du[1], Jingming Yao[1], Xinyu Liu[2], Zhaoyu Rong[1], Baiyu Guo[1], Ruyue Fang[3], Yong Su[4], Claude Delmas[5], Stephen J. Harris[6], Marnix Wagemaker[7], Liqiang Zhang[1,*], Yongfu Tang[1,*], Sulin Zhang[3,*], Lingyun Zhu[2,*], and Jianyu Huang[1,4,*]

[1]Clean Nano Energy Center, State Key Laboratory of Metastable Materials Science and Technology, Yanshan University, Qinhuangdao, China

[2]Guilin Electrical Equipment Scientific Research Institute Co., Ltd., Guilin, China.

[3]Department of Engineering Science and Mechanics, The Pennsylvania State University, University Park, PA 16802, USA

[4]Key Laboratory of Low Dimensional Materials and Application Technology of Ministry of Education, School of Materials Science and Engineering, Xiangtan University, Xiangtan, China

[5]ICMCB-CNRS, Université de Bordeaux, 33608 Pessac Cedex, France

[6]Energy Storage Division, Lawrence Berkeley, National Laboratory, Berkeley, CA 94720, USA

[7]Section Storage of Electrochemical Energy, Department of Radiation Science and Technology, Faculty of Applied Sciences, Delft University of Technology, Delft 2629 JB, The Netherlands

* Corresponding Author

E-mail: lqzhang@ysu.edu.cn (L. Q. Zhang), tangyongfu@ysu.edu.cn (Y. F. Tang), suz10@psu.edu (S. L. Zhang), zhuly@glesi.com.cn (L. Y. Zhu), and jyhuang8@hotmail.com (J. Y. Huang)

Abstract

The rock-salt phase (RSP) formed on the surface of Ni-rich layered cathodes in liquid-electrolyte lithium-ion batteries is conceived to be electrochemically "dead". Here we show massive RSP forms in the interior of $LiNi_xMn_yCo_{(1-x-y)}O_2$ (NMC) crystals in sulfide based all solid state batteries (ASSBs), but the RSP remains electrochemically active even after long cycles. The RSP and the layered structure constitute a two-phase mixture, a material architecture that is distinctly different from the RSP in liquid electrolytes. The tensioned layered phase affords an effective percolation channel into which lithium is squeezed out of the RSPs by compressive stress, rendering the RSPs electrochemically active. Consequently, the ASSBs with predominant RSP in the NMC cathode deliver remarkable long cycle life of 4000 cycles at high areal capacity of 4.3 mAh/cm^2. Our study unveils distinct mechano-electrochemistry of RSPs in ASSBs that can be harnessed to enable high energy density and durable ASSBs.

1. Introduction

Ni-rich layered cathodes such as $LiNi_xMn_yCo_{(1-x-y)}O_2$ (NMC, x≥0.5) are widely used in electrical vehicle batteries because of their high energy density. [1-5] In liquid electrolytes, a rock-salt phase (RSP) of ~30-200 nm thick forms on the surface of NMC, which impedes Li^+ transport, thus causing severe rate limiting and capacity decay. [6] Indeed, the RSP is deemed electrochemically "dead". Recently, it has been unveiled that the lattice mismatch between the RSP and the layered phase effectively blocks Li^+ extraction out of the layered phase at high state of charge, further supporting the electrochemically inactive nature of the RSP. [7] While the detrimental effect of the RSPs in LELIBs has become clear, its roles in all-solid-state batteries (ASSBs) remain unexplored.[8]

Here we show that a massive RSP formed in the bulk of NMC721 after 4000 cycles (abbreviated as NMC721-4000 hereafter) in sulfide based ASSBs. Strikingly, in contrast to the surface RSP in LELIBs, this bulk RSP does not cause significant capacity decay. In fact, after 4000 cycles, the NMC721 based ASSBs still retains a capacity of 77%. When cycled at 0.2C, the NMC721-4000 can still deliver a remarkable capacity of 138 mAh/g, which is comparable to the capacity of the pristine NMC721 cycled at the same rate and current density. Furthermore, the NMC721-4000 survives without any trace of cracks, which is in sharp contrast to the NMC cycled in LELIBs, in which cracking is ubiquitous. [9] The major defects in the NMC721-4000 are pitting and oxygen precipitation. Interestingly, oxygen release not only causes cavity formation in the NMC721 but also spills over to the surrounding LSPSCl electrolyte, causing enormous void formation in the LSPSCl. These observations suggest that the electrochemistry, chemomechanics and degradation mechanisms of NMC in ASSBs may be distinctly different from that in LELIBs, and thus warrant further investigation.

2. Results and Discussion

2.1 Materials Characterization

X-ray diffraction (XRD) indicates that the pristine NMC721 has a hexagonal structure with a space group of R-3m and a lattice parameter of a = 2.878 Å and c = 14.19 Å (Fig. S1a). Scanning electron microscopy (SEM) images of the pristine NMC721 particle indicate a particle size ranging from 3 to 7 μm (Fig. S1b-c). A cross sectional high-angle annular dark field - scanning

electron microscopy (HAADF-STEM) image of the pristine NMC721 particles shows the radially assembled grains with a size ranging from 200 to 500 nm and have some large cavities in the centers (Fig. S1d). Energy dispersive X-ray (EDX) mapping indicates that Ni, Co, Mn and O are uniformly distributed in the particle (Fig. S1e-j). Moreover, a thin layer of $LiNbO_3$ with a thickness of 10 nm was coated around the NMC721 particles (Fig. S1j). Previous studies indicate that coating of $LiNbO_3$ on the surface of NMC can not only reduce the interfacial impedance between NMC and the sulfide solid electrolyte (SE), but also prevent the reaction between LSPSCl SE and the NMC particles. The HAADF-STEM image exhibits a perfect layered structure with a lattice spacing of 4.93 Å for the (003) plane (Fig. S1k). XRD pattern of the LSPSCl SE exhibits a cubic structure with a space group of F-43m and a lattice parameter of a = 9.88 Å similar to that of the reference Li_7PS_6 (Fig. S2). The ionic conductivity of the LSPSCl SE is $3.0 * 10^{-3}$ S/cm.

2.2 Electrochemical Performance of the ASSBs

The battery was assembled in a homemade mold with LSPSCl as SE, Li-In as the anode, and NMC721 as the cathode (Fig. S3a-c, detailed cell assembly is shown in the Supporting Information). LSPSCl powders were pressed into pellets under different pressures in a mold. NMC721 cathode active materials (CAMs) were mixed with LSPSCl powders with a mass ratio of 7:3 and pressed into pellets. Li foils were placed on top of the In foil and were used as the anode. The CAM, the SE and the Li-In pellets were then pressed together in a mold to assemble the ASSBs. The cross-section SEM image shows an intimate solid-solid contact among the SE, the CAM and the Li-In anode in the ASSBs (Fig. S4a-c), and the corresponding EDX mapping shows clearly distinct cathode, anode and electrolyte layers (Fig. S4d).

The electrochemical performances were evaluated at a voltage window of 2.7-4.3 V (*vs.* Li^+/Li) at room temperature. At 1C and a high NMC721 mass loading of 36 mg/cm^2, the charge/discharge profiles (Fig. 1a) show very limited shape changes after long cycling. The NMC721 electrode delivered a discharge capacity of 116 mAh/g with an initial Coulombic efficiency (CE) of 76%. The ASSBs exhibit superior areal capacity (compared with previously reported results [10-12]) at high cathode mass loadings. It provides comparable areal capacities to commercial LELIBs (typically > 4 mAh/cm^2). [13-14] The NMC721 electrode exhibits a high initial areal capacity of 4.3 mAh/cm^2 with a capacity retention of 82% after 2000 cycles (Fig. 1b), and

4

77% even after 4000 cycles (Fig. 1c). Moreover, when the C-rate was switched to 0.2C (0.8 mA/cm^2) after 4001 cycles, the NMC721-4000 delivered a remarkable capacity of 138 mAh/g, which is comparable to the 1st cycle capacity of the pristine NMC721 cycled at the same rate and current density (Fig. 1d-e). Upon cycling at 3C (11.5 mA/cm^2), the NMC721-4000 discharge capacity was 58 mAh/g, and when cycled at 1C again, the discharge capacity was 91 mAh/g, close to the specific capacity of 88.6 mAh/g at the 4001th cycle at 1C (Fig. 1d-e). To the best of our knowledge, these results represent the longest cycle life achieved at a high areal capacity and high mass loading (Fig. 1f). [10-12, 15-17]

2.3 Microstructure characterization of the ASSBs

SEM images of the ASSB after 4000 cycles indicate a straight and smooth LSPSCl/CAM interface (Fig. 2a and Fig. S5a). EDX mapping indicates a sharp interface between the LSPSCl and the CAM (Fig. S5b). The NMC721 particles after 4000 cycles maintained good integrity (Fig. S6), and the secondary NMC721 particles were intact even after 4000 cycles (Fig. S7). High magnification SEM images reveal a distinct interfacial transition layer with a thickness of about 1 μm between the LSPSCl and the NMC721-4000 particle, and the transition layer exhibits darker contrast than both the LSPSCl and the NMC721-4000 (Fig. 2b-c). Each NMC721-4000 is surrounded by a transition layer (Fig. S8-10), which is also reflected in a 3D image (Fig. S11). EDX mapping indicates that the interfacial transition layer is O-rich but S-deficient (Fig. S12). Detailed inspection of the transition layer indicates numerous voids with size ranging from 20 to 300 nm. The contrast of the interface between the NMC721-4000 particle and the transition layer is sharp while that between the transition layer and the LSPSCl is somewhat blunt, indicating that the transition layer is located in the LSPSCl layer (Fig. 2d-e). Note that there is virtually no visible voids or cracks in the NMC721-4000 particles near the transition layer. There are many large cavities in the center of the NMC721-4000 particles which existed in the pristine sample (Fig. S1d). The absence of fracture and cracking in the NMC721 primary particles after long cycling of ASSBs is in sharp contrast to the ubiquitous cracking of NMC particles in LELIBs after cycling [18-24]. We attribute this difference to the high stack pressure and the special structure design of NMC721, where many large cavities existed in the center of the NMC721 particles, which facilitate stress release and suppress cracking during cycling.

5

EDX mapping further confirms that the transition layer is located in the LSPSCl, not in the NMC721-4000 particle (Fig. 2f-g and Fig. S13a-b), and the transition layer is deficient in S, P, Si, Cl. Moreover, high O content and trace amount of Ni and Co are also detected in the transition layer, and Mn has slipped out of the transition layer and reaches to the inner LSPSCl SE. The presence of O, Ni, Co in the transition layer and Mn in the SE ascertains that transition metal dissolution into the sulfide SE has taken place. The selected area electron diffraction (SAED) result indicates the O, Ni, Co elements in the transition layer exist in the form of Ni_2O_3 (JCPDS No. 14-0481) and Co_2O_3 (JCPDS No. 02-0770) nanoparticles (Fig. S14a-e). To the best of our knowledge, this is the first report of transition metal dissolution in SE, a phenomenon that is prevalent is LELIBs [25-27].

The microstructure of the NMC721-4000 was characterized by electron microcopy. TEM image indicates a particle with a size ranging of about 5 µm comprising of many secondary particles of 200 to 500 nm (Fig. 3a). There are large pores in the center of the primary particles, which are from the pristine samples (Fig. S1e). Detailed inspection of individual secondary particles reveals massive nanovoids or corrosion pits with sizes ranging from 5 to 10 nm and crack-like dark stripes parallel to one another (Fig. 3b-c, Fig. S15a-b and Fig. S16a-d). EDX mapping indicates that the nanopores are rich in S, suggesting diffusion of S into the nanopores (Fig. 3d). Atomic resolution HAADF-STEM and annular bright field-scanning electron microscopy (ABF-STEM) images indicate that the bulk of the NMC721-4000 exhibits RSP rather than the layered structure, indicating that a massive phase transformation from a layered structure to a rock-salt structure after 4000 cycles has occurred (Fig. 3e, e-1, e-2 and e-3). We estimate from several representative HAADF-STEM images that the proportion of the RSP and disordered layered phases are over 70% in the NMC721-4000 (Fig. S17a-d). HAADF-STEM images indicate that the crack-like dark stripes are interconnected nanopores which aligned along the (003)/(111) planes of the layered/RSP phases (Fig. 3f and Fig. S18). HAADF-STEM and ABF-STEM images indicate that the nanopores (Fig. 3g, g-1 and g-2) or stripes (Fig. 3h) are actually not empty but filled with RSP despite significant mass loss. Note that the RSPs are nucleated from the nanovoids surface in the interior of the NMC particles (Fig. 3g and Fig. S19a-b). RSP formation on the surface of Ni-rich layered cathode has been widely reported in LELIBs and ASSBs (Fig. S20a-c), however, RSP formation in the bulk of Ni-rich layered cathode has not been reported. [28] The RSP in the NMC721-4000 is distinctly different from that observed in the

NMC in LELIB: the RSP in the former is massive and mixed with the layered structure (e.g. Fig. 3e), which dominates the structure of the entire NMC721-4000 particles. In contrast, the RSP in the latter exists predominantly on the surface of the NMC particle with a thickness of usually ~20-200 nm.

Although the NMC721-4000 is dominated by RSP, when it was cycled at 0.2C after 4001 cycles, it delivered an astonishing 138 mAh/g specific capacity, which is comparable to that of the pristine NMC cycled at the same electrochemical conditions. When cycled at 3C and 1C, it also delivered capacities of 58 and 91 mAh/g, proving conclusively the RSP is electrochemically active.[29-31]

In LELIBs, the RSP is formed via two different mechanisms. [32] In the first, the interaction of the liquid electrolyte with the surface of NMC causes O stripping from NMC, leading to the formation of RSP; [33-35] in the second, over delithiation induces under-coordinated transition metals, which become unstable and migrate to the Li conduction layer, forming the RSP. [36] In ASSBs, we revealed the nucleation of RSP from the interior of the NMC particle, and majority of the NMC particle has been converted to RSP, suggesting that the second mechanism seen in LELIBs is mostly active in ASSBs.

It is unexpected that upon the majority of the layered structure has been converted to RSP, the ASSBs still delivered impressive capacity. More astonishingly, when cycled at low rate, the RSP phase delivered a capacity comparable to that of the pristine layered NMC, proving unambiguously the electrochemical active nature of the RSP, which is opposite to the conventional view that the RSP is electrochemically dead. In fact, previous report showed that only less than 10% of RSP may lead to 50% capacity loss of LELIBs, [33, 37-41] which leads to the view that in such RSP Li$^+$ diffusion channel is completely blocked. [42] However, it was speculated that disordered RSP may exhibit electrochemical activity. [28, 43-44] It was proposed that a percolating network for Li$^+$ diffusion in $Li_{1.211}Mo_{0.467}Cr_{0.3}O_2$ with a lithium-excess cation disordered phase can be formed, and density functional theory (DFT) calculation suggests that Li$^+$ diffusion in the Li-percolating network is energetically feasible in the lithium-excess cation-disordered rock-salt type structure.[28]

To resolve the controversial views regarding the electrochemical activity of the RSPs, we turn to mechanics analyses based on the differential material architecture of the RSPs formed in liquid and solid electrolytes (Fig. 4, Fig. S21 and Fig. S22). [45] In liquid electrolytes, RSPs form

primarily at the electrode/electrolyte interface covering the active layered phase at the interior of NMC particles, forming a core-shell like structure during cycling. It is known that the dense RSP layer considerably slows down Li^+ diffusion. More importantly, lattice mismatch between the RSP and the layered phase generates compressive stress in the RSP layer and tension in the layered phase, as shown in Fig. 4a by our finite element analysis. The compressive stress further retards and may even completely blocks Li^+ diffusion at high state of charge. [46-49] As a result, the thick, compressed RSPs functions as an impermeable layer, trapping all the remaining Li^+ in the layered phase, causing considerable capacity loss. The large tensile stress may well exceed the strength of the layered structure, causing fracture, as widely reported by previous studies.

Differently, in ASSBs disordered RSPs are dispersed in the layered phase, forming a 3D mixture. A layer of RSP also forms at the electrode/electrolyte interface; this layer (~ 2 nm), however, is much thinner than that in liquid electrolytes ($\sim 20 - 200$ nm). The lattice mismatch between the RSP and the layered phase still situates the RSPs in compression and the layered phases in tension (Fig. 4b). During charging, the stress gradient between the phases drives Li^+ from the RSP to adjacent layered phase and nanopores, much like squeezing water out of wet clothes. The connected nanopores and the layered phase form a percolation channel, facilitating Li^+ transport out of the NMC particles, thus maintaining a large capacity albeit low kinetics. The externally applied stack pressure superimposes onto the lattice mismatch induced stress field, increasing the compression in RSPs but reducing the tension in layered structure. This asymmetric stress state inhibits crack nucleation and propagation, setting the NMC particle on a mechanically safe mode. [50]

Owing to the relative compliance of the surrounding SEs in comparison to the NMC particles, the chemical potential of oxygen molecules released from the RSP transformation in SE is much lower than inside the NMC particles. The chemical potential gradient drives the oxygen diffusion and insertion into the SEs, leaving vacancies and nanopores near the RSPs on the one hand and forming the transition layer in the SEs on the other.

3. Conclusion

In conclusion, our study reveals distinct electrochemistry of RSPs in ASSBs from LELIBs: electrochemically dead in the latter but active in the former. We attribute the different electrochemical activeness of the RSPs to the phase architecture and the accompanying

mechanics. While the lattice mismatch generally causes RSPs in compression and the layered structures in tension, the different phase architectures of the formed RSPs lead to distinct mechanical effects on Li$^+$ transport, detrimental in LELIBs but beneficial in ASSBs. Moreover, we reveal that the unique phase architecture and chemomechanics in ASSBs afford the NMC cathodes high cracking resistance, which is further pronounced when high stack pressure is applied. These findings provide new understanding to the chemomechanics and electrochemistry of ASSBs that can be effectively harnessed to enable high energy density and durable ASSBs, which hold great promise for electrical vehicle applications.

4. Experimental Section

4.1. Assembly of Li-In/LSPSCl/NMC721 ASSBs

a. Electrolyte layer fabrication: The $Li_{10}Si_{0.3}PS_{6.7}Cl_{1.8}$ (LSPSCl) solid electrolyte (SE) powders were purchased from GLESI Corp., CHINA. A 70 mg LSPSCl powder with a particle size of 1 to 10 μm was poured into a Teflon tube with a diameter of 10 mm, and then cold-pressed at a pressure of 380 MPa to obtain an electrolyte pellet with a thickness of ~400 μm (Fig. S3a).

b. Cathode fabrication: The polycrystalline $LiNi_{0.7}Co_{0.2}Mn_{0.1}O_2$ (NMC721) powders were produced by GLESI, CHINA. NMC721 cathode particles with sizes ranging from 3 to 7 μm, which were coated by a $LiNbO_3$ layer with a thickness of 10 nm, were mixed with LSPSCl powders in a weight ratio of 7:3 using an agate mortar and a pestle. The mixture of cathode and LSPSCl was then placed on the top of the LSPSCl electrolyte pellet and pressed at a preparation pressure (P_C) of 1220 MPa (Fig. S3b).

c. Anode preparation: A thin lithium foil with a thickness of 50 μm was pressed on an indium (In) foil of 50 μm under a processing pressure (P_c) of 760 MPa at the bottom of an electrolyte layer to form a Li-In electrode, and then a battery test was performed at a stack pressure (P_S) of 760 MPa (Fig. S3c).

4.2. Electrochemical measurements

a. Galvanostatic charge and discharge measurements of the batteries were conducted on a LAND CT-2001A (Wuhan LAND Electronic Co.Ltd., Wuhan, China) battery test system in a glove box under Ar atmosphere at room temperature. The ASSBs were first charged to 4.3 V (*vs.* Li$^+$/Li) at

9

a constant current of 1C (1C = 150 mAh/g) and then remained at a constant voltage of 4.3 V (*vs.* Li$^+$/Li) for 15 min. During the discharge process, the ASSBs were discharged to 2.7 V (*vs.* Li$^+$/Li) at the same current of 1C at room temperature.

4.3. Postmortem characterizations

a. X-ray diffraction (XRD, Rigaku D/MAX-2500, Japan) was carried out to characterize the material structure in the range from 10° to 90° with a step of 5°/min, using Cu Kα radiation. To avoid air exposure, the samples were protected by an amorphous film in a glove box with water and oxygen contents less than 0.1 ppm.

b. To obtain SEM images of the cross-section of the ASSBs, the ASSBs was polished using a cross section polisher (JEOL, IB-19520CCP, Japan). The ASSBs were then placed on SEM stubs and transferred to the FIB-SEM using a home-made sample transition tool kit. Cross sectional characterizations of the ASSBs were performed using focused ion beam and scanning electron microscopy (FIB-SEM, Helios G4 CX, Thermo Fisher Scientific). Energy dispersive X-ray (EDX, Thermo Fisher Scientific) mapping was used to analyze the chemical composition of the cross sections of the ASSBs and the interface between NMC721 and LSPSCl. During the transfer process, the samples were not exposed to the air. The samples for scanning transmission electron microscopy (STEM) observations with a thickness of 60 nm were fabricated by FIB under a 2-30 kV Ga$^+$ ion beam with a current of 44 nA to 14 pA. The FIB prepared samples were characterized by a STEM (Themis Z, Thermo Fisher Scientific) at 300 kV with a condenser lens spherical aberration (Cs) corrector (CEOS GmbH). The collection semiangles of the STEM detectors were set to 65-200 mrad for high angle annular dark field (HAADF) imaging, and 8-17 mrad for annular bright field (ABF) imaging. To avoid serious specimen damage and obtain reliable images, the beam current was adjusted to be as low as possible (40-65 pA).

CRediT authorship contribution statement

Zaifa Wang, Zhenyu Wang, Dingchuan Xue, Jun Zhao, Xuedong Zhang, Lin Geng, Yanshuai Li, Congcong Du, Jingming Yao, Xinyu Liu, Zhaoyu Rong, Baiyu Guo, Ruyue Fang, and **Yong Su**: Conceptualization, Methodology, Validation, Data analysis, Investigation. **JianYu Huang**, **Sulin Zhang**, and **Zaifa Wang**: Writing – original draft. **JianYu Huang**, **Sulin**

Zhang, **Lingyun Zhu**, **Liqiang Zhang**, and **Yongfu Tang**: Conceptualization, Methodology, Data analysis, Investigation, Writing – review & editing. **Zhaoyu Rong** and **Xinyu Liu**: Methodology, Data analysis. **JianYu Huang**, **Yongfu Tang**, **Sulin Zhang, Liqiang Zhang,** and **Lingyun Zhu**: Supervision, Project administration. **Claude Delmas**, **Stephen J. Harris,** and **Marnix Wagemaker**: Writing – review & editing.

Declaration of Competing Interest

The authors declare no competing financial interest.

References

(1)   J. Kim, H. Lee, H. Cha, M. Yoon, M. Park, J. Cho, Prospect and reality of Ni-rich cathode for commercialization, *Advanced energy materials 8* (2018), 1702028.

(2)   W. Li, E. M. Erickson, A. Manthiram, High-nickel layered oxide cathodes for lithium-based automotive batteries, *Nature Energy 5* (2020), 26-34.

(3)   A. Manthiram, B. Song, W. Li, A perspective on nickel-rich layered oxide cathodes for lithium-ion batteries, *Energy Storage Materials 6* (2017), 125-139.

(4)   S. T. Myung, F. Maglia, K. J. Park, C. S. Yoon, P. Lamp, S. J. Kim, Y. K. Sun, Nickel-rich layered cathode materials for automotive lithium-ion batteries: achievements and perspectives, *ACS Energy Letters 2* (2017), 196-223.

(5)   H.-J. Noh, S. Youn, C. S. Yoon, Y.-K. Sun, Comparison of the structural and electrochemical properties of layered Li[$Ni_xCo_yMn_z$]O_2 (x= 1/3, 0.5, 0.6, 0.7, 0.8 and 0.85) cathode material for lithium-ion batteries, *Journal of power sources 233* (2013), 121-130.

(6)   H. Zhang, H. Liu, L. F. J. Piper, M. S. Whittingham, G. Zhou, Oxygen Loss in Layered Oxide Cathodes for Li-Ion Batteries: Mechanisms, Effects, and Mitigation, *Chemical Reviews 122* (2022), 5641-5681.

(7)   C. Xu, K. Märker, J. Lee, A. Mahadevegowda, P. J. Reeves, S. J. Day, M. F. Groh, S. P. Emge, C. Ducati, B. Layla Mehdi, Bulk fatigue induced by surface reconstruction in layered Ni-rich cathodes for Li-ion batteries, *Nature Materials 20* (2021), 84-92.

(8)   C. Wang, S. Hwang, M. Jiang, J. Liang, Y. Sun, K. Adair, M. Zheng, S. Mukherjee, X. Li, R. Li, H. Huang, S. Zhao, L. Zhang, S. Lu, J. Wang, C. V. Singh, D. Su, X. Sun, Deciphering Interfacial Chemical and Electrochemical Reactions of Sulfide-Based All-Solid-State Batteries, *Advanced Energy Materials 11* (2021), 2100210.

(9)   H.-H. Ryu, B. Namkoong, J. H. Kim, I. Belharouak, C. S. Yoon, Y.-K. Sun, Capacity fading mechanisms in Ni-rich single-crystal NCM cathodes, *ACS Energy Letters 6* (2021), 2726-2734.

(10)   X. Li, Q. Sun, Z. Wang, D. Song, H. Zhang, X. Shi, C. Li, L. Zhang, L. Zhu, Outstanding electrochemical performances of the all-solid-state lithium battery using Ni-rich layered oxide cathode and sulfide electrolyte, *Journal of Power Sources 456* (2020), 227997.

(11)   D. H. Tan, Y. T. Chen, H. Yang, W. Bao, B. Sreenarayanan, J. M. Doux, W. Li, B. Lu, S. Y. Ham, B. Sayahpour, Carbon-free high-loading silicon anodes enabled by sulfide solid electrolytes, *Science 373* (2021), 1494-1499.

(12)   L. Zhou, T. T. Zuo, C. Y. Kwok, S. Y. Kim, A. Assoud, Q. Zhang, J. Janek, L. F. Nazar, High areal capacity, long cycle life 4 V ceramic all-solid-state Li-ion batteries enabled by chloride solid electrolytes, *Nature Energy* (2022), 1-11.

(13)   D. Lin, Y. Liu, Y. Cui, Reviving the lithium metal anode for high-energy batteries, *Nature Nanotechnology 12* (2017), 194-206.

(14)   S.-H. Park, P. J. King, R. Tian, C. S. Boland, J. Coelho, C. Zhang, P. McBean, N. McEvoy, M. P. Kremer, D. Daly, J. N. Coleman, V. Nicolosi, High areal capacity battery electrodes enabled by segregated nanotube networks, *Nature Energy 4* (2019), 560-567.

(15)   X. Fan, G. Hu, B. Zhang, X. Ou, J. Zhang, W. Zhao, H. Jia, L. Zou, P. Li, Y. Yang, Crack-free single-crystalline Ni-rich layered NCM cathode enable superior cycling performance of lithium-ion batteries, *Nano Energy 70* (2020), 104450.

(16)   L. Ye, X. Li, A dynamic stability design strategy for lithium metal solid state batteries, *Nature 593* (2021), 218-222.

(17)   Y. Zhang, X. Sun, D. Cao, G. Gao, Z. Yang, H. Zhu, Y. Wang, Self-Stabilized $LiNi_{0.8}Mn_{0.1}Co_{0.1}O_2$ in thiophosphate-based all-solid-state batteries through extra LiOH, *Energy Storage Materials 41* (2021), 505-514.

(18)   P. Yan, J. Zheng, M. Gu, J. Xiao, J. G. Zhang, C. M. Wang, Intragranular cracking as a critical barrier for high-voltage usage of layer-structured cathode for lithium-ion batteries, *Nature communications 8* (2017), 1-9.

(19)   J. Vetter, P. Novák, M. R. Wagner, C. Veit, K. C. Möller, J. Besenhard, M. Winter, M. Wohlfahrt Mehrens, C. Vogler, A. Hammouche, Ageing mechanisms in lithium-ion batteries, *Journal of power sources 147* (2005), 269-281.

(20)   H. Liu, M. Wolf, K. Karki, Y. S. Yu, E. A. Stach, J. Cabana, K. W. Chapman, P. J. Chupas, Intergranular cracking as a major cause of long-term capacity fading of layered cathodes, *Nano Letters 17* (2017), 3452-3457.

(21)   W. S. Yoon, K. Y. Chung, J. McBreen, X. Q. Yang, A comparative study on structural changes of $LiCo_{1/3}Ni_{1/3}Mn_{1/3}O_2$ and $LiNi_{0.8}Co_{0.15}Al_{0.05}O_2$ during first charge using in situ XRD, *Electrochemistry Communications 8* (2006), 1257-1262.

(22)   v. C. Pouillerie, L. Croguennec, C. Delmas, The $Li_xNi_{1-y}Mg_yO_2$ (y= 0.05, 0.10) system: structural modifications observed upon cycling, *Solid State Ionics 132* (2000), 15-29.

(23)   B. Mortemard de Boisse, D. Carlier, M. Guignard, L. Bourgeois, C. Delmas, $P_2-Na_xMn_{1/2}Fe_{1/2}O_2$ Phase Used as Positive Electrode in Na Batteries: Structural Changes Induced by the Electrochemical (De) intercalation Process, *Inorganic chemistry 53* (2014), 11197-11205.

(24)   U. H. Kim, H. H. Ryu, J. H. Kim, R. Mücke, P. Kaghazchi, C. S. Yoon, Y. K. Sun, Microstructure-controlled Ni-rich cathode material by microscale compositional partition for next-generation electric vehicles, *Advanced energy materials 9* (2019), 1803902.

(25)   E. McCalla, A. M. Abakumov, M. Saubanère, D. Foix, E. J. Berg, G. Rousse, M.-L. Doublet, D. Gonbeau, P. Novák, G. Van Tendeloo, Visualization of O-O peroxo-like dimers in high-capacity layered oxides for Li-ion batteries, *Science 350* (2015), 1516-1521.

(26)   A. Manthiram, W. Choi, Suppression of Mn dissolution in spinel cathodes by trapping the protons within layered oxide cathodes, *Electrochemical and solid-state letters 10* (2007), A228.

(27)   A. R. Armstrong, M. Holzapfel, P. Novák, C. S. Johnson, S.-H. Kang, M. M. Thackeray, P. G. Bruce, Demonstrating oxygen loss and associated structural reorganization in the lithium battery cathode Li[Ni$_{0.2}$Li$_{0.2}$Mn$_{0.6}$]O$_2$, *Journal of the American Chemical Society 128* (2006), 8694-8698.

(28)   J. Lee, A. Urban, X. Li, D. Su, G. Hautier, G. Ceder, Unlocking the potential of cation-disordered oxides for rechargeable lithium batteries, *science 343* (2014), 519-522.

(29)   M. Oishi, C. Yogi, I. Watanabe, T. Ohta, Y. Orikasa, Y. Uchimoto, Z. Ogumi, Direct observation of reversible charge compensation by oxygen ion in Li-rich manganese layered oxide positive electrode material, Li$_{1.16}$Ni$_{0.15}$Co$_{0.19}$Mn$_{0.50}$O$_2$, *Journal of Power Sources 276* (2015), 89-94.

(30)   M. D. Radin, S. Hy, M. Sina, C. Fang, H. Liu, J. Vinckeviciute, M. Zhang, M. S. Whittingham, Y. S. Meng, A. Van der Ven, Narrowing the gap between theoretical and practical capacities in Li-ion layered oxide cathode materials, *Advanced Energy Materials 7* (2017), 1602888.

(31)   J. Xu, M. Sun, R. Qiao, S. E. Renfrew, L. Ma, T. Wu, S. Hwang, D. Nordlund, D. Su, K. Amine, Elucidating anionic oxygen activity in lithium-rich layered oxides, *Nature communications 9* (2018), 1-10.

(32)   H. Zhang, H. Liu, L. F. Piper, M. S. Whittingham, G. Zhou, Oxygen Loss in Layered Oxide Cathodes for Li-Ion Batteries: Mechanisms, Effects, and Mitigation, *Chemical Reviews* (2022).

(33)   F. Lin, I. M. Markus, D. Nordlund, T. C. Weng, M. D. Asta, H. L. Xin, M. M. Doeff, Surface reconstruction and chemical evolution of stoichiometric layered cathode materials for lithium-ion batteries, *Nature communications 5* (2014), 1-9.

(34)   F. Lin, D. Nordlund, I. M. Markus, T. C. Weng, H. L. Xin, M. M. Doeff, Profiling the nanoscale gradient in stoichiometric layered cathode particles for lithium-ion batteries, *Energy & Environmental Science 7* (2014), 3077-3085.

(35)   D. Qian, B. Xu, M. Chi, Y. S. Meng, Uncovering the roles of oxygen vacancies in cation migration in lithium excess layered oxides, *Physical Chemistry Chemical Physics 16* (2014), 14665-14668.

(36)   R. A. House, U. Maitra, L. Jin, J. G. Lozano, J. W. Somerville, N. H. Rees, A. J. Naylor, L. C. Duda, F. Massel, A. V. Chadwick, What triggers oxygen loss in oxygen redox cathode materials?, *Chemistry of Materials 31* (2019), 3293-3300.

(37)   S. Hwang, W. Chang, S. M. Kim, D. Su, D. H. Kim, J. Y. Lee, K. Y. Chung, E. A. Stach, Investigation of changes in the surface structure of Li$_x$Ni$_{0.8}$Co$_{0.15}$Al$_{0.05}$O$_2$ cathode materials induced by the initial charge, *Chemistry of Materials 26* (2014), 1084-1092.

(38)   S. K. Jung, H. Gwon, J. Hong, K. Y. Park, D. H. Seo, H. Kim, J. Hyun, W. Yang, K. Kang, Understanding the degradation mechanisms of LiNi$_{0.5}$Co$_{0.2}$Mn$_{0.3}$O$_2$ cathode material in lithium ion batteries, *Advanced Energy Materials 4* (2014), 1300787.

(39)   B. B. Lim, S. J. Yoon, K. J. Park, C. S. Yoon, S. J. Kim, J. J. Lee, Y. K. Sun, Advanced concentration gradient cathode material with two-slope for high-energy and safe lithium batteries, *Advanced Functional Materials 25* (2015), 4673-4680.

(40)   W. Zhao, J. Zheng, L. Zou, H. Jia, B. Liu, H. Wang, M. H. Engelhard, C. Wang, W. Xu, Y. Yang, J. Zhang, High Voltage Operation of Ni-Rich NMC Cathodes Enabled by Stable Electrode/Electrolyte Interphases, *Advanced Energy Materials 8* (2018), 1800297.

(41)   H. Zhang, F. Omenya, M. S. Whittingham, C. Wang, G. Zhou, Formation of an Anti-Core–Shell Structure in Layered Oxide Cathodes for Li-Ion Batteries, *ACS Energy Lett. 2* (2017), 2598-2606.

(42)   Y. Lyu, L. Ben, Y. Sun, D. Tang, K. Xu, L. Gu, R. Xiao, H. Li, L. Chen, X. Huang, Atomic insight into electrochemical inactivity of lithium chromate ($LiCrO_2$): Irreversible migration of chromium into lithium layers in surface regions, *Journal of Power Sources 273* (2015), 1218-1225.

(43)   A. Urban, J. Lee, G. Ceder, The configurational space of rocksalt-type oxides for high-capacity lithium battery electrodes, *Advanced Energy Materials 4* (2014), 1400478.

(44)   R. Wang, X. Li, L. Liu, J. Lee, D. H. Seo, S. H. Bo, A. Urban, G. Ceder, A disordered rock-salt Li-excess cathode material with high capacity and substantial oxygen redox activity: $Li_{1.25}Nb_{0.25}Mn_{0.5}O_2$, *Electrochemistry Communications 60* (2015), 70-73.

(45)   K. Momma, F. Izumi, VESTA 3 for three-dimensional visualization of crystal, volumetric and morphology data, *Journal of applied crystallography 44* (2011), 1272-1276.

(46)   M. Gu, H. Yang, D. E. Perea, J.-G. Zhang, S. Zhang, C.-M. Wang, Bending-induced symmetry breaking of lithiation in germanium nanowires, *Nano letters 14* (2014), 4622-4627.

(47)   S. Kim, S. J. Choi, K. Zhao, H. Yang, G. Gobbi, S. Zhang, J. Li, Electrochemically driven mechanical energy harvesting, *Nature communications 7* (2016), 1-7.

(48)   X. H. Liu, F. Fan, H. Yang, S. Zhang, J. Y. Huang, T. Zhu, Self-limiting lithiation in silicon nanowires, *Acs Nano 7* (2013), 1495-1503.

(49)   T. Chen, P. Zhao, X. Guo, S. Zhang, Two-Fold Anisotropy Governs Morphological Evolution and Stress Generation in Sodiated Black Phosphorus for Sodium Ion Batteries, *Nano Letters 17* (2017), 2299-2306.

(50)   Y. Qi, C. Ban, S. J. Harris, A new general paradigm for understanding and preventing Li metal penetration through solid electrolytes, *Joule 4* (2020), 2599-2608.

Figure captions
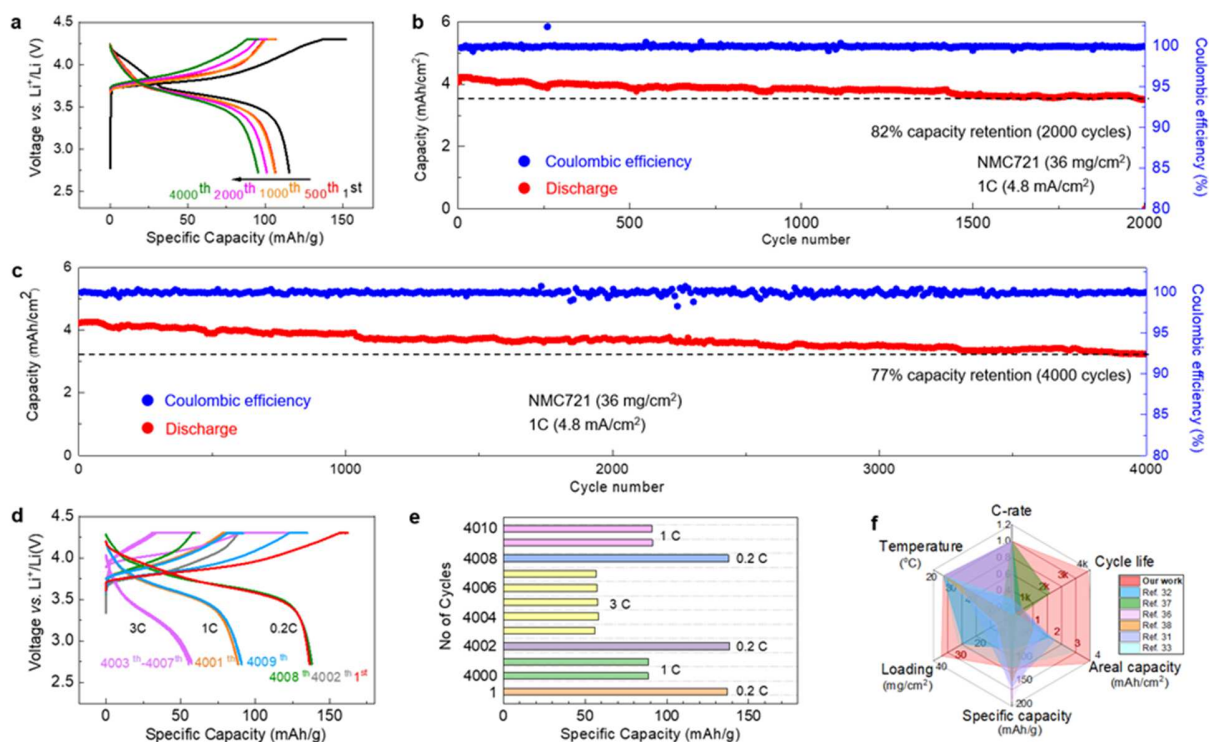
Fig. 1. Electrochemical measurements of the ASSBs. Voltage profiles (a), charge/discharge capacity and the Coulombic efficiency for NMC721 after 2000 cycles (b) and after 4000 cycles (c). Voltage profiles (d) and rate capability (e) of NMC721 after 4000 cycles. (f) Comparison of the performance of ASSBs with that in literature.
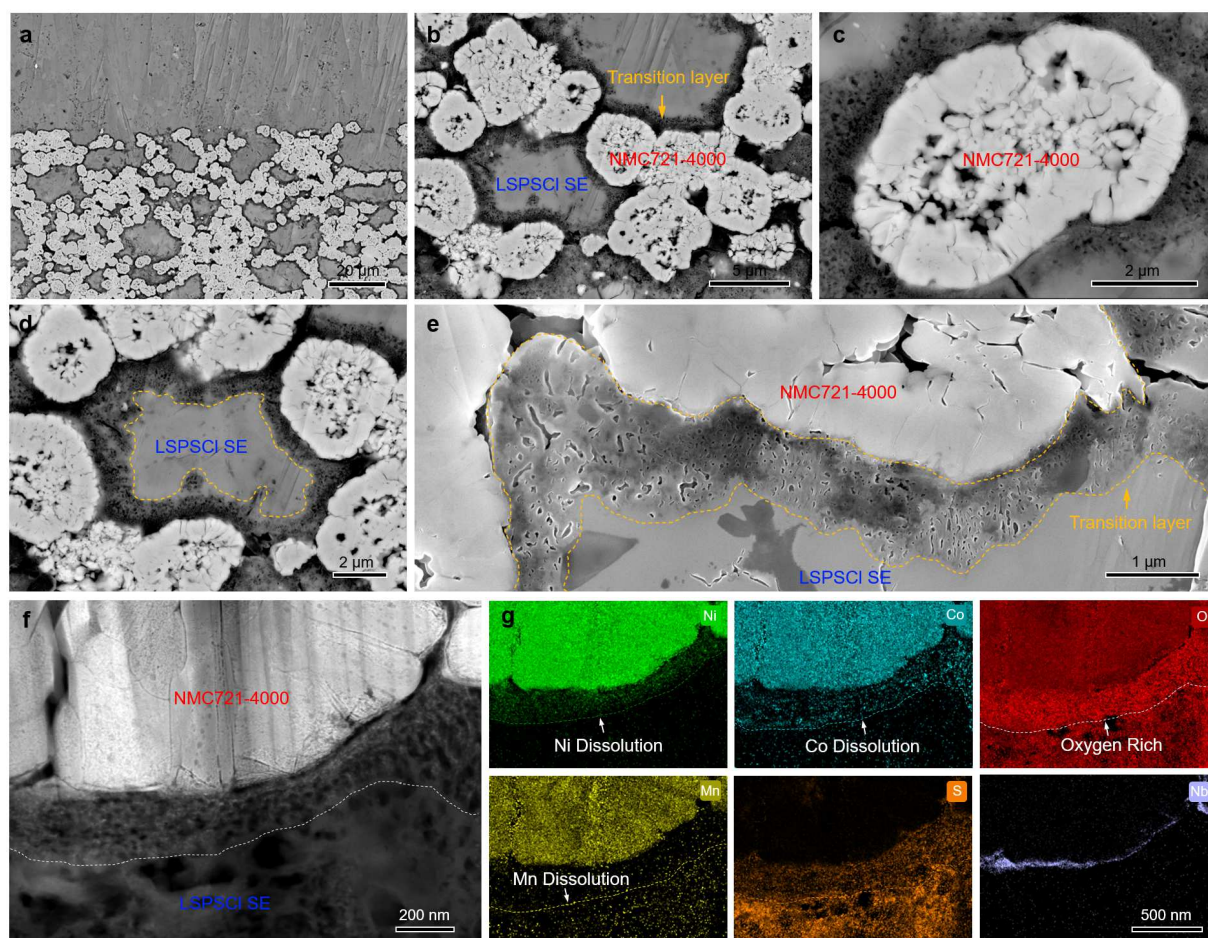
Fig. 2. SEM characterization of the LSPSCl/NMC721 interfaces after 4000 cycles. (a) A low magnification SEM image of the LSPSCl/NMC721 interface. (b) A SEM image of the NMC721/LSPSCl interface, showing a transition layer with darker contrast than the NMC721 and the SE. (c-d) SEM images of the NMC721 particle and its surrounding transition layer. (e) A high magnification SEM image showing the massive voids in the transition layer. A SEM image of NMC721 and its surrounding transition layer (f), and the corresponding EDX mapping (g).
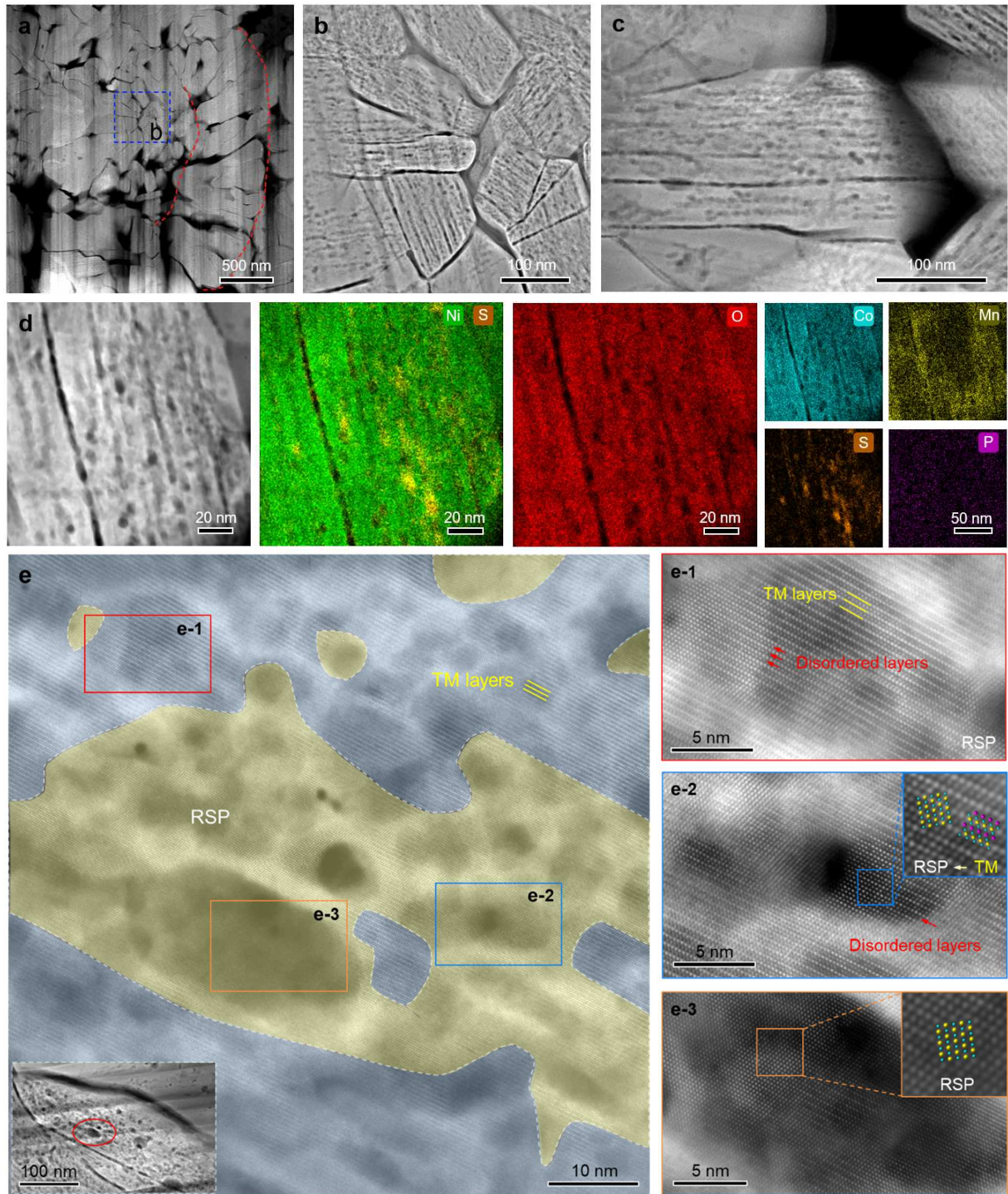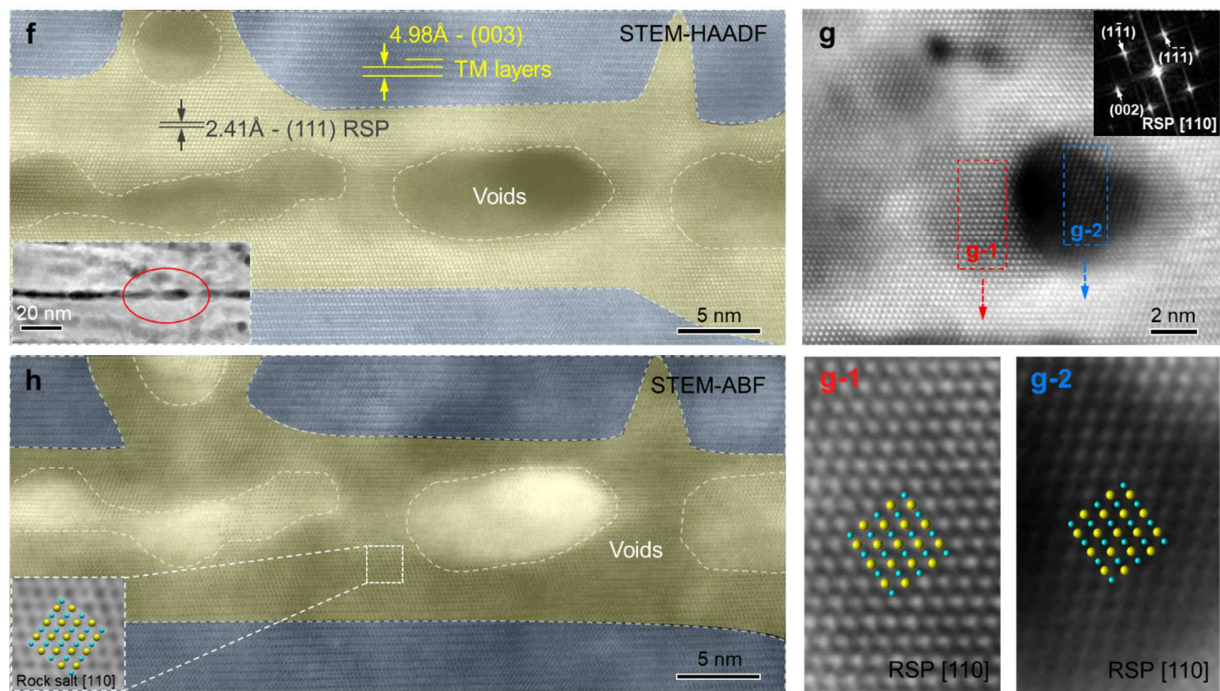
Fig. 3. STEM characterization of the NMC721 after 4000 cycles. (a) A low magnification STEM-HAADF image of the NMC721-4000 particle, showing numerous large voids preexisted in the pristine particle. (b-c) STEM-HAADF images of the NMC721-4000 particle, showing the massive nano voids and dark stripes in the secondary particles. (d) EDX mapping of a NMC721-4000 particle with nano voids and stripes. (e) STEM-HAADF showing the majority of the NMC721-4000 particle has been converted to RSP. STEM-HAADF (f-g), and ABF (h) images showing the voids lined up along the (111) RSP/ (003) layered cathode. The RSPs are nucleated in the interior of a NMC721-4000 particle. All the voids are filled with RSPs.
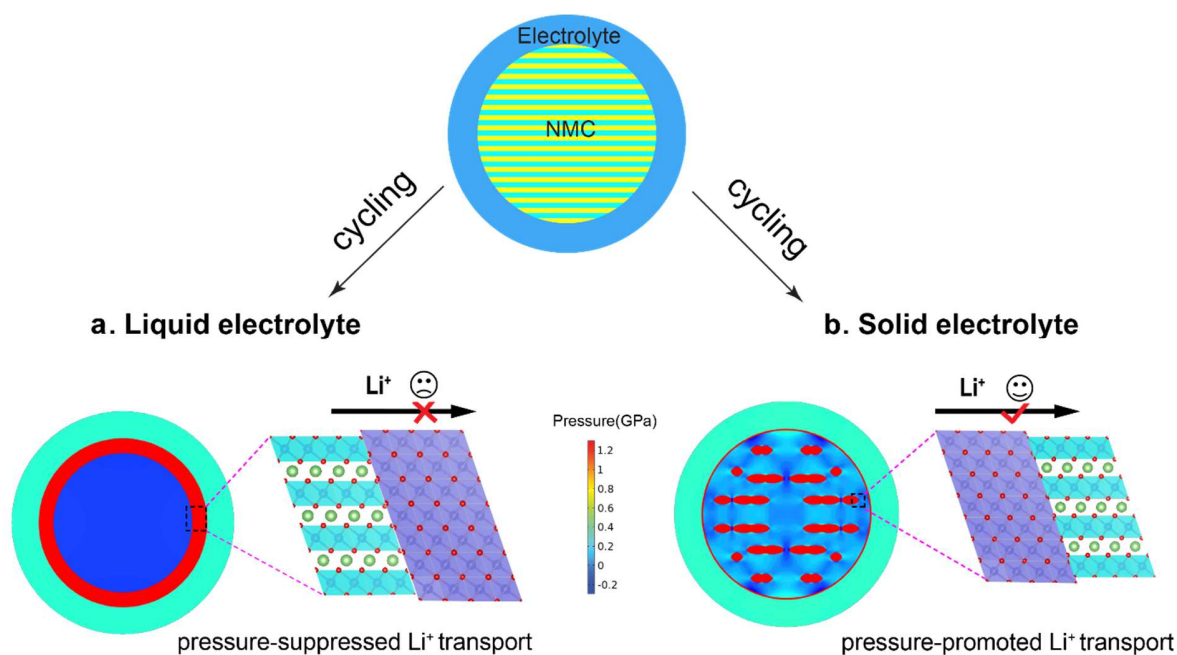
Fig. 4. Stress-mediated Li$^+$ transport kinetics in liquid and solid electrolytes. (a) In liquid electrolytes, electrochemical cycling forms a thick RSP (~20-200 nm) at the NMC/electrolyte interface. The lattice mismatch between the phases generates compression in the RSPs (red) and tension in the layered structures (blue). The dense, highly compressed RSPs function as an impermeable layer that traps all the remaining Li$^+$ in the interior layered phases, causing considerable capacity loss. (b) In solid electrolytes, electrochemical cycling forms RSPs that are dispersed into the bulk of the NMC particle. The compressive stress in the RSPs (red) squeezes Li$^+$ out of the RSPs into the adjacent layered phases (light blue/blue), and the layered phases form a percolation channel that conducts Li$^+$ further out of the NMC particle, rendering an electrochemically active RSPs.

Reviving the rock-salt phases in Ni-rich layered cathodes by mechano-electrochemistry in all-solid-state batteries

Graphical Abstract

Massive rock-salt phase (RSP) dispersed in the layered phase of $LiNi_{0.7}Co_{0.2}Mn_{0.1}O_2$ (NMC721) cathode is formed in sulfide based all-solid-state batteries (ASSBs) after 4000 cycles. Counter to the prevailing belief that RSP is electrochemically "dead", the RSP in ASSBs is fully electrochemically active due to the synergistic effect of the percolation of the layered phase and the compressive stress on the RSP.